The Cryosphere
Discussions

Cast shadows reveal changes in glacier thickness

Monika Pfau[1], Georg Veh[1], Wolfgang Schwanghart[1]

[1]Department of Environmental Sciences and Geography, University of Potsdam, Potsdam, 14476, Germany

Correspondence to: Monika Pfau (monika.pfau@arcor.de)

5   **Abstract.** Increased rates of glacier retreat and thinning call for accurate local estimates of glacier elevation change to predict future changes in glacier runoff and their contribution to sea level rise. Glacier elevation change is typically derived from digital elevation models (DEMs) tied to surface change analysis from satellite imagery. Yet, the rugged topography in mountain regions can cast shadows onto glacier surfaces, making it difficult to detect local glacier elevation changes in remote areas. However, most optical satellite images offer precise time-stamped meta data of the solar position and angle during the

10   acquisition. These data are useful to simulate shadows from a given DEM. Accordingly, any differences in shadow length between simulated and mapped shadows in satellite images could indicate a change in glacier elevation relative to the acquisition date of the DEM. We tested this hypothesis at five selected glaciers with long-term monitoring programs. For each glacier, we projected cast shadows on the glacier surface from freely available DEMs and compared simulated shadows to cast shadows mapped in ~40 years of Landsat images. We validated the relative differences with *in situ* geodetic measurements of

15   glacier elevation change. We find that shadow-derived glacier elevation changes are consistent with independent photogrammetric and geodetic surveys in shadowed areas. Our method shows that Baltoro Glacier (Karakoram, Pakistan) gained slightly in elevation between1987 and 2020, while Great Aletsch Glacier (Switzerland) recorded the most negative thinning rates of about 1 m per year. Our approach provides local glacier thickness changes, a vital information to quantify possibly varying elevation-dependent changes in the accumulation or ablation zone of a given glacier. Shadow-based retrieval

20   of glacier elevation changes hinges on the precision of the DEM as the geometry of ridges and peaks constrain the shadow that we cast on the glacier surface. Future generations of DEMs with higher resolution and accuracy will improve our method, enriching the toolbox for tracking historical glacier mass balances from satellite and aerial images especially in remote glacier areas with difficult field access.

1 Introduction

25

Quantifying spatial and temporal patterns of glacial changes is important to understand the response of the cryosphere to ongoing atmospheric warming (IPCC 2019). Changes in glacier volume determine the availability of regional and local freshwater resources that support the basic needs of many millions of people living in glaciated river basins (IPCC 2019; Pritchard 2019; Azam et al. 2021). Glacier retreat can shift ecosystems higher in elevation, changing the composition of, and possibly creating new, habitats (Brighenti et al. 2019; Cauvy-Fraunié and Dangles 2019). Shrinking glaciers also alter discharge seasonality, enhance rates of sediment transport, and shift biogeochemical and contaminant fluxes in glaciated river basins (Li et al. 2021; Milner et al. 2017). In high mountains, glacier retreat can also destabilize adjacent hillslopes, possibly enhancing the frequency and magnitude of catastrophic slope failures (Huggel et al. 2012). Other hazards to mountain communities evolve from new meltwater lakes that can suddenly empty in glacial lake outburst floods (Veh et al. 2020). Recent appraisals entail that ice loss has accelerated globally in past decades, with thinning rates of glaciers outside the Antarctic and Greenland ice sheets having doubled between 2000 and 2019 (Hugonnet et al. 2021). Still, some 141,000 km³ of glacier ice cover ~10% of the Earth's land surface today (Farinotti et al. 2019; Millan et al. 2022). Given projected future warming scenarios, sustainable management of these remaining ice resources requires accurate knowledge of regional and local mass balances (Richardson and Reynolds 2000; Bolch et al. 2011).

30

35

Measuring changes in the surface elevations of glaciers relies on repeated field and remote sensing based surveys. Space-borne techniques such as laser altimetry (ICESat) (Moholdt et al. 2010; Neckel et al. 2014), radar interferometry (Farías-Barahona et al. 2020) or stereo-photogrammetry (Bolch et al. 2011) helped quantify changes in glacier surface elevation over large spatial scales and in terrain which is difficult to access. These appraisals are largely constrained to the past two decades, with few exceptions such as Corona and Hexagon missions, which provided one-time stereo image pairs between the 1960s and 1970s (Lovell et al. 2018; Dehecq et al. 2020). Other space-borne derived estimates of long-term glacier changes have relied on time series of optical satellite images, yet without the capability of using stereo-photogrammetry. The Landsat mission has been particularly useful for mapping changes in glacier area, rather than elevation, primarily due to continuous recording period extending back to the 1970s, the high temporal repetition rate of 16 days, and a moderate spatial resolution of 30 m (Paul et al. 2011; Wulder et al. 2019; Wulder et al. 2022). If intersected with a DEM, glacier outlines mapped in Landsat (or any other satellite or aerial) images can help reveal changes in glacier elevation (Zhang et al. 2016; Rankl and Braun 2016).

40

45

50

While optical satellite and aerial imagery provides the longest, remotely sensed records of glacier change, its analysis is challenging in topographic settings where high relief casts shadows on highly reflective glacier surfaces (Kääb et al. 2016). As mountains block the direct incoming solar radiation, shadowed glacier surfaces are characterized by a low variation of radiometric values, thus complicating visual image interpretation or automated approaches of image classification (Richter 1998; Paul et al. 2002; Racoviteanu and Williams 2012; Li et al. 2016). The problem of cast shadows increases with latitude owing to seasonal differences in solar elevation angle, and with the height of mountains, as those can cast wider shadows.

55

Against these known limitations, we hypothesize that cast shadows in optical satellite images also have a largely untapped potential for mapping glacier elevation changes. If the local glacier elevation has changed in two successive time steps, the shape of shadows emanating from adjacent mountains has to change accordingly, as long as solar elevation, azimuth, and the

60 geometry of ridges and peaks remain constant (Fig. 1). Therefore, we expect that glacier thinning must locally cause longer shadows, while a local gain in glacier thickness will shorten the length of shadows. Using the tangent, the horizontal offset can be converted into a vertical displacement, i.e. a change in elevation. These changes in elevation can also be translated into estimates of glacier altitude using a digital elevation model (DEM) as a reference (Fig. 1).
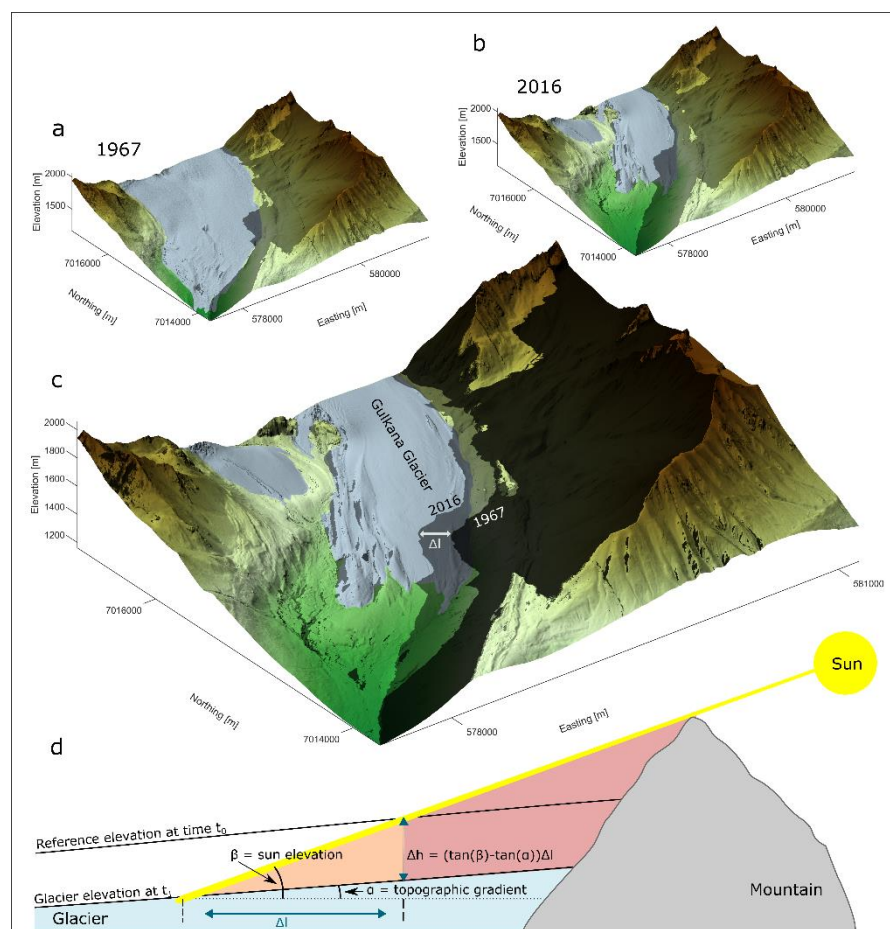

65 **Figure 1: Effects of changing glacier elevation on the length of cast shadows.** Example of modelled shadows on Gulkana Glacier, Alaska, using digital elevation models and mapped glacier outlines in two distinct years from McNeil et al (2022). **a,** DEM from, and surface area (light blue) of, Gulkana Glacier in 1967. **b,** DEM from, and surface area of, Gulkana Glacier in 2018. **c**, DEM from 2018 with shadows from 1967 and 2018. Shadows were calculated based on a sun elevation of 20° and sun azimuth of 135°. The horizontal difference between the shadows (arrow in **c**) is 210 m. **d,** Diagram of the trigonometric relationship that predicts longer horizontal shadows under a constant sun
70 elevation β and mountain topography, assuming that the glacier maintains its topographic gradient α. In the example, the gain in shadow length at the terminus of the Gulkana Glacier translates into a glacier elevation change of ca. -76 m.

Previous studies that use single-look imagery to detect glacier elevation changes are scarce. One recent attempt assessed ice-shelf freeboard heights and the height of volcanic plumes (Rada Giacaman 2022). Yet, the potential of the shadow-height method in glacier geodetic surveys has remained unaddressed on a broader geographic range. Here we address the question of
75   how well, or if at all, we can measure topographic changes on glaciers based on the variability of shadows cast by surrounding mountains. To this end, we develop and test an approach that applies trigonometry to time series of shadows extracted from Landsat satellite images, draped over local DEMs, in order to identify local glacier surface changes. We validate this method at five glaciers for which we have detailed information on local mass-balance and topographic changes.

2 Study sites

80   We selected five glaciers in North America, Europe, and Central Asia, spanning 20° of latitude (Fig. 2). Our selection was guided by the availability of long (decadal) time series of glacier mass balances, high-resolution DEMs, and glacier outlines, providing a validation to our analysis. The shadows cast on these glaciers account for varying sun angles and surrounding relief, and occur in accumulation as well as ablation areas. The Great Aletsch Glacier is located in the Swiss Alps, offering one of the longest consecutive records of mass balances in this mountain region (Bauder et al. 2007). The summit of
85   Dreieckhorn casts a pronounced shadow on the Great Aletsch Firn at ~2,950 m a.s.l., which is close to the estimated equilibrium line altitude (ELA) of 2,961 m during the period of 1971-1990 (Zemp et al. 2007). High and steep mountains surround Baltoro Glacier in Pakistan. The Mitre Peak creates a nearly triangular shadow near Concordia (~4,500 m a.s.l.), which is the confluence of Baltoro and Godwin-Austen Glacier. This shadow is likely in the ablation zone, given an ELA at ~5,200 m a.s.l. (Minora et al. 2015). The northern-most glacier in our study is Gulkana (Alaska, USA), shaded twice by Ogive Mountain at
90   ~1,850 m a.s.l. and Icefall Peak at ~1,800 m a.s.l.. We did not study the shadow near the tongue of Gulkana Glacier, given that most Landsat images are acquired at noon when shadows are absent or very small. The ELA of Gulkana Glacier ranged from 1,811 m a.s.l. to 2,178 m a.s.l. between 2009 and 2019 (McNeil et al. 2022), such that the shadows were largely in the ablation zone. On South Cascade Glacier (Washington, USA), the shadow of Lizard Mountain shows two peaks, which form one coherent shadow on the glacier (~2,050 m a.s.l.). This shadow is above the ELA, which ranges between 1,794 and 2,042 m
95   a.s.l. (1986 to 2018) (McNeil et al. 2022). Finally, Sperry Glacier (Montana, USA) is shadowed at an altitude of ~2,350 m a.s.l. by Gunsight Mountain. The shadow is situated largely in the ablation zone, given an average ELA at ~2,500 m a.s.l. for the period 2005-2019 (McNeil et al. 2022).
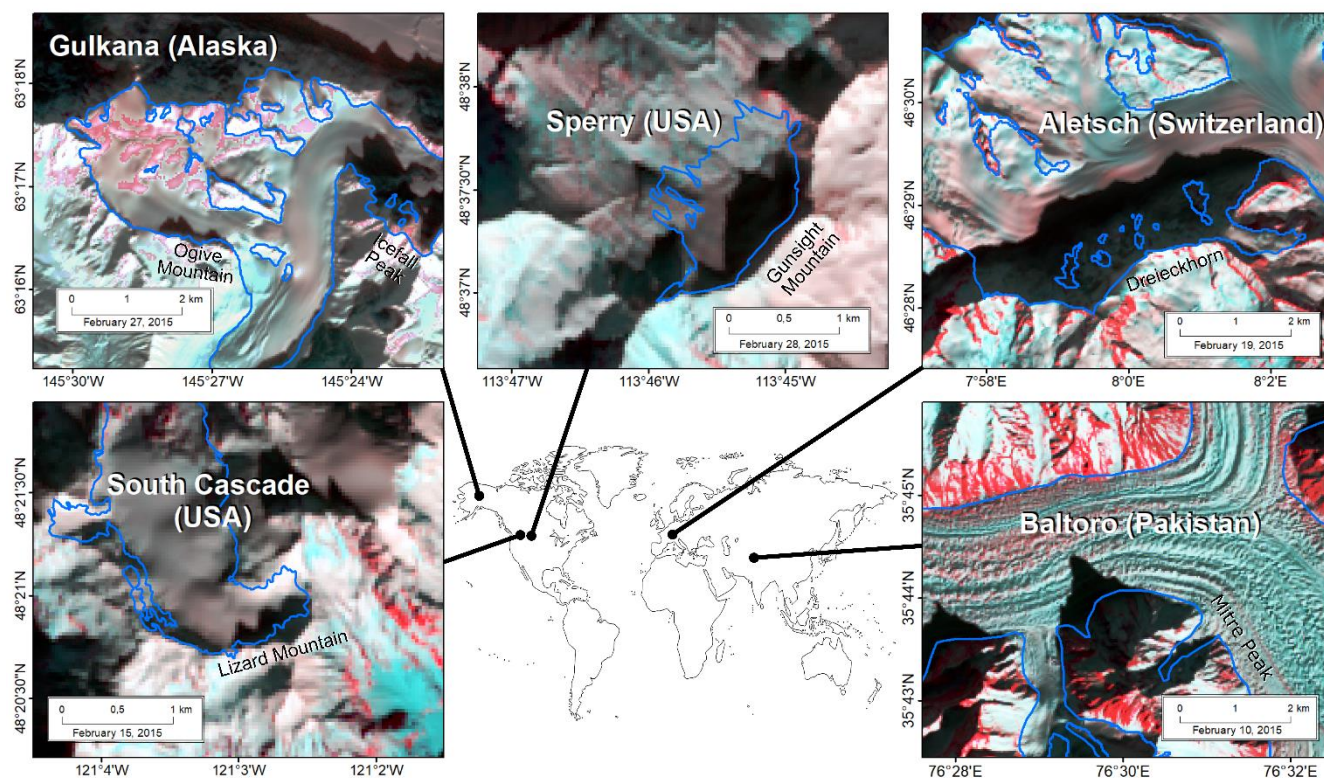
Figure 2: Map of the five study regions. Images are false-color composites (SWIR, blue, and green bands) from Landsat OLI obtained in
February 2015. Blue polygons are the glacier outlines in the Randolph Glacier Inventory, V6.0.

3 Data and methods

3.1. Satellite images and DEMs

We obtained 30-m resolution Landsat images (level L1TP-Precision and Terrain corrected) to map shadows within
the glacier surface. To this end, we downloaded 60 cloud-free Landsat images (41 from TM, two from ETM+, and 17 from
OLI) with acquisition period between 1986 and 2020 from the USGS *EarthExplorer* (https://earthexplorer.usgs.gov/,
Appendix A1).

We used several DEMs (see Table A2) to simulate cast shadows for the dates at which the Landsat images were
acquired. For four glaciers, we used the DEM of the Shuttle Radar Topography Mission (SRTM-1), which has a spatial
resolution of 30 m (Farr et al. 2007). For Gulkana Glacier, we used the ArcticDEM (acquisition year 2009, 2 m spatial
resolution) given that this glacier is located beyond the maximum acquisition range of SRTM at 60° North. Owing to high
vertical uncertainties in SRTM data in rough topography (Mukul et al. 2017), we also used a number of other DEMs to enhance
and validate our results. For Great Aletsch Glacier, we obtained the swissALTI3D DEM (acquisition year 2019, downsampled

to 5 m spatial resolution by merging multiple raster datasets). For Baltoro Glacier, we modified the SRTM-1 so that the mountains are replaced with data from the Viewfinder Panoramas (VFP) project (De Ferranti 2015). VPF data mainly consists

115 of SRTM data but has been filled and corrected with other sources where voids or artefacts due to phase unwrapping errors within the SRTM data occur. We merged both DEMs because we wanted to keep the glacier from the original SRTM DEM as its survey date is known to be the year 2000, while the date of the map basis of VFP is not known to us. The latter has little impact on our analysis because we assume the elevation of mountain ridges to remain unchanged during our study period.

120 **3.2. Workflow for estimating trends in glacier elevation change in shaded areas**

We created a binary mask of shaded and non-shaded areas (Fig. 3a) by applying a user-defined threshold to the digital numbers of the green band (encompassing a wavelength of 525-600 nm) of each Landsat scene (Appendix A1). We found the green band suitable because shadows appear dark on the otherwise bright glacier surface. For each Landsat image, we obtained the sun azimuth and sun elevation from the associated metadata file. We used these parameters of the sun position to simulate

125 cast shadows using a ray-tracing algorithm available in SAGA-GIS V2.3.2 (Conrad et al. 2015). This algorithm returns a binary raster classifying each pixel either as shaded or non-shaded, equivalent to our threshold-based mapping (Fig. 3b). We then calculated the difference in area between the modelled and manually mapped shadow, and clipped the resulting polygons to the glacier outline in the Randolph Glacier Inventory (Pfeffer et al. 2014) (Fig. 3c). Within these difference polygons, we obtained the change in shadow length using geodetic lines at a regular spacing of 30 m (i.e. the cell size of Landsat images) in

130 the direction of the sun azimuth (Fig. 3d–f, Appendix A1). These lines represent the incoming sun rays and are assumed to be parallel, given that the Sun is a distant, point-shaped light source and the change in shadow length is considered relatively short compared to the distance between Earth and Sun. Artefacts in the geodetic lines (Fig. 3d) appeared mainly because of the limited resolution of the DEM and satellite images (i.e. interruption of lines by pixel corners or shadow bottom edge and hole phenomenon), such that we removed them manually. Finally, we used the trigonometric relationship of the law of tangents

135 to convert the length of each line to changes in elevation relative to the date when the DEM was acquired (Fig. 1).
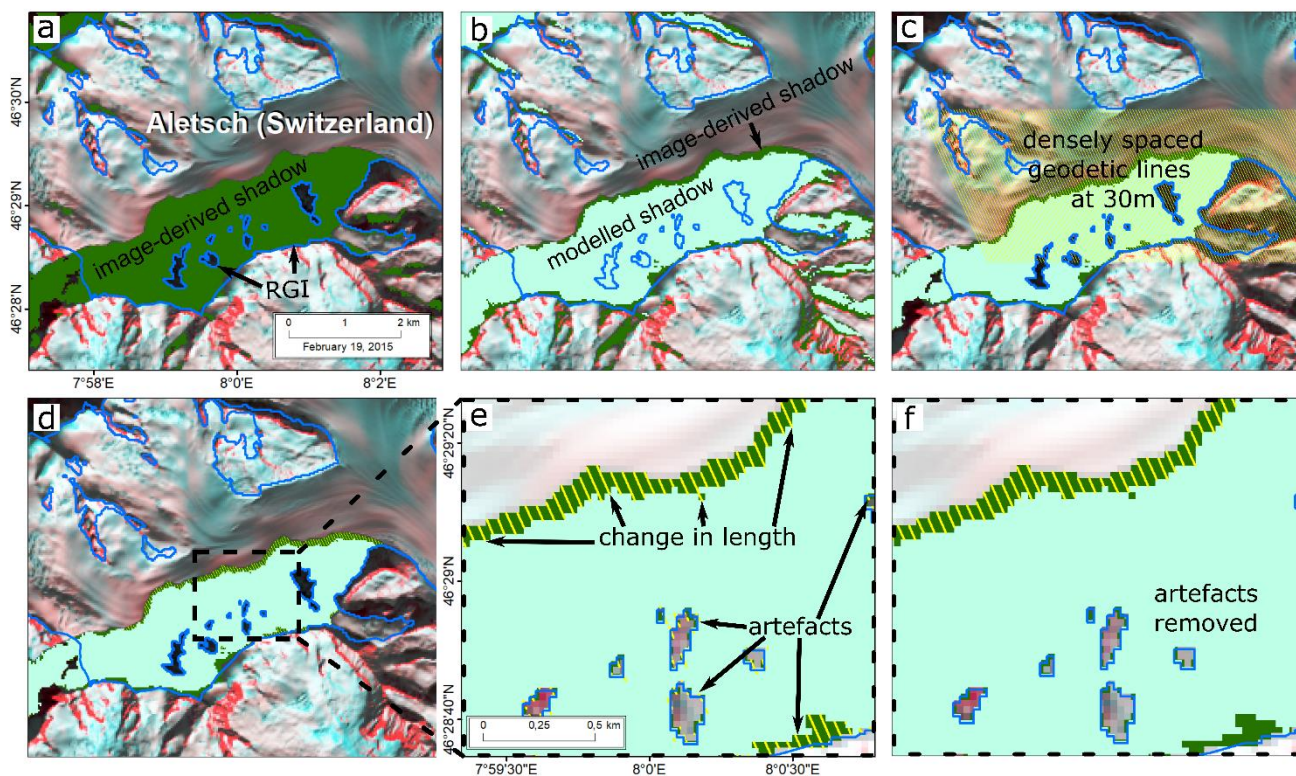
Figure 3: Flowchart of modelling terrain shadows using the example of Great Aletsch glacier. (a) Shadows mapped (green) using a threshold of 5500 in the Landsat 8 image (using false-color composite in the SWIR, blue, and green bands) together with Randolph Glacier Inventory (RGI), **(b)** Modelled shadow (turquoise) using SAGA-GIS, draped over the mapped shadow in the Landsat image, **(c)** Extracted shadows by RGI and pattern of parallel geodetic lines, **(d)** Lines cut to the difference between the two shadows, **(e)** Close up of d with generated lines of change in shadow length and unwanted artefacts, **(f)** Artefacts at the bottom edge and along cut outs are removed.

We used a Bayesian multi-level linear regression model to estimate the trend in elevation change for each glacier with time. Multi-level models can accommodate groups in data, in our case different glaciers, within a single model. We can thus estimate local effects at a given glacier with respect to the entire population learned from all data regardless of their location. Multi-level models improve parameter estimates for individual groups, in particular when differing sample sizes cause variance across the groups (McElreath 2020). This feature is advantageous in our analysis as the number of geodetic lines per year differs strongly among glaciers. The model learns the population-level parameters from the data, which serve as shared prior distributions for each group. In this way, the glaciers inform each other, reducing uncertainty in years with few geodetic lines at a given glacier. The parameters in the model are drawn from distributions specified by population-level (hyper-) parameters, which are also learned from the data. The multi-level model returns the posterior distribution for both population-level and group-level parameters.

Our likelihood function follows a Student's t-distribution, which is robust against outliers (Kruschke 2014). We modelled the trend in glacier elevation change Δh with year y as

155

$$\Delta h_{ji} \sim t(\mu_{ji}, \kappa, \nu), \text{ for } j = 1, \dots, J \text{ and } i = 1, \dots, n_j \tag{1}$$

$$\mu_{ji} = \alpha_j + \beta_j y_{ji}, \text{ for } j = 1, \dots, J \text{ and } i = 1, \dots, n_j \tag{2}$$

$$\begin{bmatrix} \alpha_j \\ \beta_j \end{bmatrix} \sim MVNormal \left[\begin{pmatrix} \alpha \\ \beta \end{pmatrix}, \mathbf{S} \right] \tag{3}$$

$$S = \begin{pmatrix} \sigma_\alpha & 0 \\ 0 & \sigma_\beta \end{pmatrix} R \begin{pmatrix} \sigma_\alpha & 0 \\ 0 & \sigma_\beta \end{pmatrix} \tag{4}$$

$$R = \begin{pmatrix} 1 & \varsigma \\ \varsigma & 1 \end{pmatrix} \tag{5}$$

160 where Δh are the elevation changes from geodetic lines in each year, i is an index for n geodetic lines, and J is the number of glaciers. The likelihood function has a location parameter μ, κ is a positive scale parameter, and ν are the degrees of freedom, fixed at $\nu = 3$. The parameters α_j and β_j are the intercepts and slopes for each group, respectively, and α and β are the corresponding parameters on population-level. The covariance matrix S is composed of group-level standard deviations σ_α and σ_β, and R, the correlation matrix with correlation ς. We choose the following priors to model the parameters for the entire

165 population and all groups (i.e. the glaciers)

$$\kappa \sim N(0, 2.5) \tag{6}$$

$$\alpha \sim N(0, 2.5) \tag{7}$$

$$\beta \sim N(0, 2.5) \tag{8}$$

$$\sigma_\alpha \sim N(0, 2.5) \tag{9}$$

170

$$\sigma_\beta \sim N(0, 2.5) \tag{10}$$

$$R \sim LkjCholesky(1). \tag{11}$$

These priors refer to standardised data pairs (Δh and y) with zero mean and unit standard deviation. Choosing wide priors with a zero-mean Gaussian and standard deviation of 2.5 admits both negative and positive trends for β, such that the posteriors are largely informed by the data. We choose a Cholesky LKJ correlation distribution prior for R, so that all

175 correlation matrices are equally likely. We numerically approximate this posterior using a Hamiltonian sampling algorithm implemented in Stan that is called via the software package brms within the statistical programming language R (Stan Development Team 2022; R Core Team 2022; Bürkner 2017). We ran three parallel chains with 6,000 iterations after 2,000

warm-up runs, and found that the Markov chains have converged ($\hat{R}$ statistic = 1.0). We report the posterior distributions of all model parameters in Table A3.

3.3 Comparison to reference DEMs and historical maps

The density of ice in shaded areas remains unknown, so we refrained from converting our data to water equivalents. Instead, we compared our estimated trends in glacier elevation change with trends calculated from high-resolution DEMs for the same shaded areas. For all glaciers in North America, we used repeated DEMs available for USGS benchmark glaciers from McNeil et al. (2022) and sampled the elevation values in polygons covering the areas around the shadow outlines. These DEMS have spatial resolutions ranging between several decimeters to 10 m, derived from historic topographic maps, aerial stereo photography, and space-borne imagery. For the Great Aletsch Glacier, we obtained glacier elevation changes from online historical maps (Siegfriedkarte at map scales of 1:25,000 and 1:50,000) available for 12 years between 1959 and 2020 from the Bundesamt für Landestopografie KOGIS (Koordination, Geoinformation und Services, https://www.swisstopo.admin.ch). To infer elevation changes from contour lines in historical maps, we manually chose four points with a spacing of 1 km along a straight line in the flow direction of the glacier within the area covered by the shaded glacier. For each map, we then extracted the glacier elevation at each point using linear interpolation and calculated the average elevation change from these points. For Baltoro Glacier, high-resolution historic elevation data for comparison are unavailable.

We use the same multi-level structure as above (Eqs. 1-11) to determine the trends in glacier elevation change from glaciers with repeat, high-resolution DEMs. To this end, we conditioned the model on $J = 4$ glaciers (excluding Baltoro), chose the same priors, and maintained the setup of the Hamiltonian sampler. We found that all chains have converged ($\hat{R} = 1.0$) and report all model parameters in Table A4.

3.4 Assessment cast-shadows from globally available DEMs

We assume that the quality of the DEM could bias our estimates of glacier elevation changes due to different spatial resolutions, artefacts, and horizontal and vertical errors (e.g. due to foreshortening, layover and shadow effects) characteristic for different DEM sources. These uncertainties propagate into modelled cast-shadows and likely affect possible trends in glacier elevation derived from different globally available DEMs (Table A2). The Great Aletsch Glacier provides six several freely available DEMs, which we used to quantitatively and qualitatively assess changes in the size and shape of the inferred shadows. From Open Topography (https://opentopography.org/), we obtained two SRTM DEMs (SRTM-1 with 30 m and SRTM-3 with 90 m spatial resolution), the NASADEM (30 m, reanalysis of SRTM data), ALOS World 3D (AW3D30 with 30 m), and two Copernicus DEMs (GLO-30 with 30 m and GLO-90 with 90 m). We compared the DEM-derived shadows to those from the LiDAR-based swissALTI3D DEM, which we treat as the benchmark. In each simulation, we use a sun azimuth of 135° and sun elevation of 30°.

4 Results

4.1 Glacier elevation changes from cast shadows

210   In each Landsat scene, $45^{+66}/_{-16}$ geodetic lines (median, 2.5% and 97.5% of the distribution) pass through the mapped shadows on the five selected glaciers (Appendix A1). Individual geodetic lines suggest the lowest variance in glacier elevation change at Sperry Glacier (-17 m/ +10 m; 2.5% and 97.5% of the distribution) and the highest variance at Baltoro Glacier (-164 m/ +66 m), when adjusting elevation changes relative to the year of the reference DEM. Our analysis of trends in glacier

215   elevation changes suggests that Great Aletsch Glacier had the highest annual rate of thinning with $-1.08^{-0.06}/_{-0.05}$ m yr^{-1} (mean and 95% highest density interval, HDI). Sperry and South Cascade Glacier lost on average about 0.4 m per year since the late 1980s. Annual rates of glacier elevation change at Gulkana Glacier are not credibly different from zero, whereas Baltoro Glacier shows slight gains in glacier thickness (Figure 4).
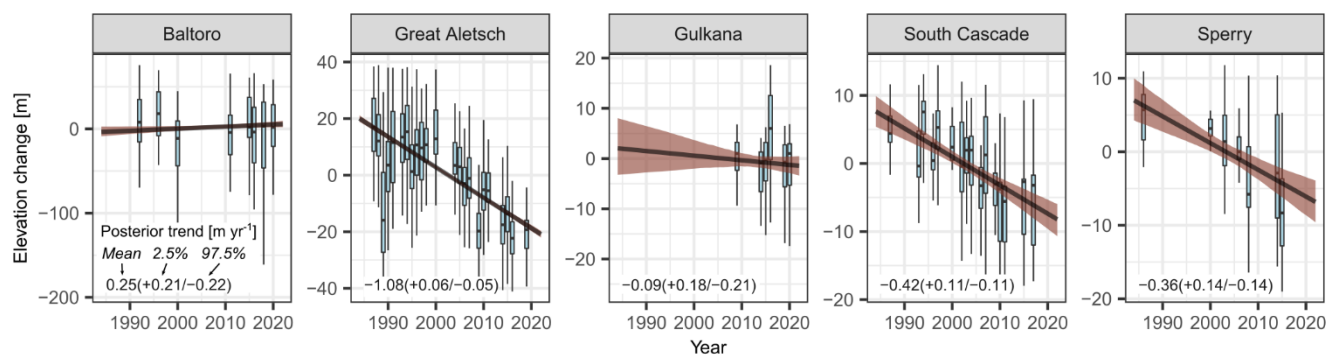

220   **Figure 4: Trends in elevation change on shaded glacier surfaces.** Boxplots show glacier elevation changes inferred from geodetic lines drawn in a given Landsat image. Values of elevation change are relative to the reference year, i.e. the year of DEM acquisition. Horizontal lines are the median, boxes encompass the interquartile range, and whiskers are 1.5 times the interquartile range. Outliers (lowest and highest percent in the distribution) are removed. Thick black line is the mean posterior trend and brown shade is the 95% highest density interval (HDI). Numbers in lower left corner summarise the posterior distribution of the trend in glacier elevation change, including the mean, the
225   lower 2.5%, and the upper 97.5% of the HDI.

4.2 Comparison with reference DEMs

Our estimated trends from geodetic lines match the trends obtained from high-resolution DEMs and historical maps (Fig. 5). However, uncertainties in the trends calculated from the reference DEMs are higher given that fewer data enter the

230   model, especially if we fit the model only to data obtained during the Landsat period. We find similar trends in mean glacier elevation change between our method and high-resolution DEMs at Great Aletsch Glacier ($-1.08^{+0.06}/_{-0.05}$ vs. $-1.07^{+0.64}/_{-0.72}$ m yr^{-1}). During the Landsat period, the mean trend from the high-resolution DEMs at South Cascade Glacier is more than twice that of the trends obtained from geodetic lines ($-1.17^{+0.57}/_{-0.57}$ vs. $-0.42^{+0.11}/_{-0.11}$ m yr^{-1}). Estimates overlap, however, if we consider all available data from South Cascade, extending back to late-1950s (Fig. 5). Note the large

10

235 uncertainties at Sperry and Gulkana Glacier, given that only two observations inform the multi-level model in each case. At Gulkana, both our method and high-resolution DEMs suggest the highest uncertainties in the estimated trends, leaving little room for a credible trend in glacier elevation change.
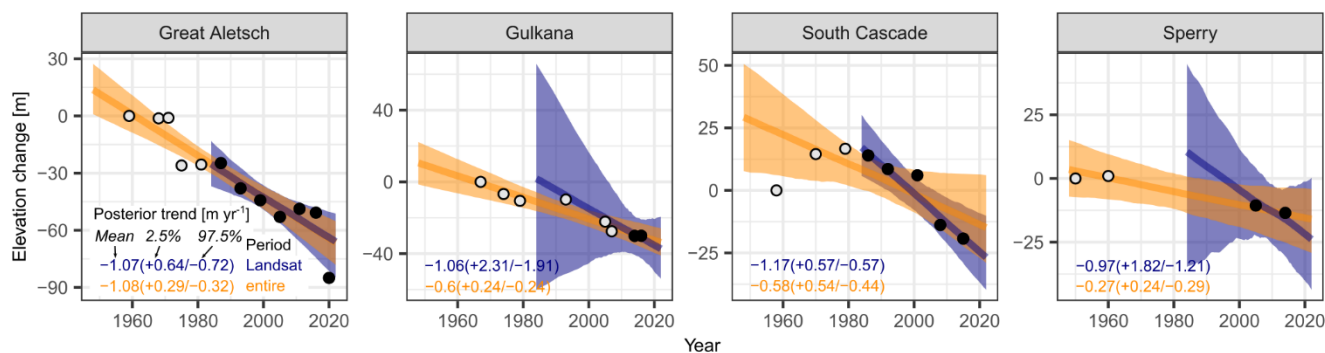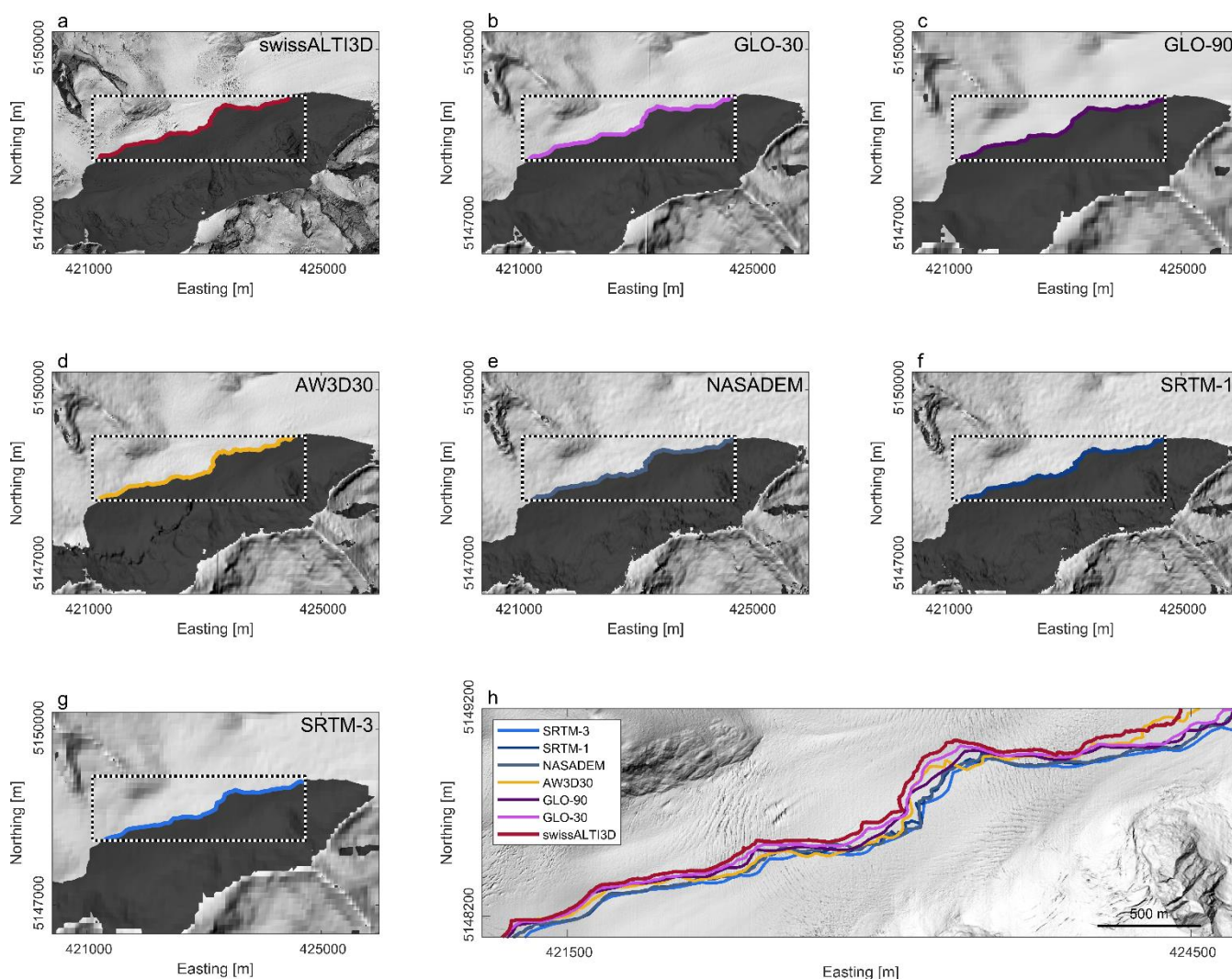

Figure 5: Reported glacier elevation changes in shadowed areas for four glaciers. All values are relative to the first observation for each glacier, which is set to zero. Black bubbles are observations when Landsat images are available for a given glacier, grey bubbles mark values before the Landsat period. Shades, thick lines, and numbers refer to the Landsat period (blue) and pre-Landsat period (orange). Numbers in lower corner left summarise the posterior distribution of the trend in glacier elevation change, including the mean, the lower 2.5%, and the upper 97.5% of the HDI.

4.3 Comparison of DEMs

The elevation changes obtained from geodetic lines have substantial variance in a given year (Fig. 4), suggesting that
245 DEM resolution and quality are important in estimating glacier elevation change from cast shadows. Indeed, the example of the Great Aletsch Glacier shows that different DEMs produce shadows of different lengths, even with constant sun azimuth and elevation (Figs. 6, 7). This variation reflects limits in the DEM resolution and the representation of ridge lines. The acquisition date may also play a role, assuming that ongoing thinning might produce longer shadows in more recent DEMs. In our example, shadows projected from swissALTI3D DEM (5 m spatial resolution, acquisition in 2017 and 2018) extend
250 farthest to the north (Fig. 6a). The large shadow area thus likely follows both from the reported decadal glacier thinning and from a more precise representation of the surrounding topography (Fig. 6a). Shadows from the GLO-30 DEM (acquisition date 2010-2015, ~30 m spatial resolution) are very similar to those derived from the swissALTI3D DEM (Figs. 6b, 7). We also find the smallest variance in shadow length for the GLO-30 DEM (Fig. 7). Shadows derived from the GLO-90 DEM (~90 m resolution) show both a larger spatial offset (Fig. 6c) as well as a higher variability in shadow length (Fig. 7). We attribute
255 this mismatch to a higher degree of spatial averaging, causing lower topographic ridges due to the coarser spatial resolution. Shadows derived from the AW3D30 DEM (acquisition period between 2006 and 2011, ~30 m spatial resolution) are highly variable compared to the swissALTI3D DEM (Fig. 6d). Some of the shadows extend beyond those derived from the swissALTI3D DEM, an effect of exaggerated topography in the DEM that overestimates the height of the ridge (Fig. 7). Finally, shadows derived from the SRTM DEMs and NASADEM (Fig. 6e-g) – all derived from data acquired from the same

260   shuttle mission in 2000 – show the highest difference to the swissALTI3D DEM. SRTM DEMs and NASADEM derived

shadows are very similar, but again, the coarser SRTM-3 DEM leads to a lowering of the ridges and larger horizontal distances.

In summary, variations in modelled shadows obtained from different DEMs relate to variable acquisition dates but also reflect

how accurately ridge topography is represented in the DEMs. Comparison of DEMs with the same acquisition date but different

spatial resolution show that coarser DEMs underestimate ridge height and commensurately shadow length. Notwithstanding,

265   a general trend towards longer shadows can be observed for younger acquisition dates (Fig. 7).

Figure 6: Shadows projected onto Great Aletsch Glacier using different digital elevation models. (a-g) Grey hillshades show the simulated cast shadow using a sun azimuth of 135° and elevation of 25°. **(h)** Close-up of the shadow outlines modelled with different DEMs.
270   Hillshade in the background is from the swissALTI3D DEM.

12

Figure 7: Difference in the lengths of geodetic lines crossing a shadow on Great Aletsch using six DEMs and the benchmark swissALTI3D DEM.

4 Discussion

275   We developed and assessed a method that allows for measuring glacier elevation changes in remote areas based on shadows casted from adjacent mountains. The precision and accuracy of the method depend on several factors that pertain to the individual processing steps and the input data (Rada Giacaman 2022). We show that DEM quality and resolution cause variability in the detected elevation changes. To this end, we assessed the length of geodetic lines that link the shadow outlines along the azimuth direction. We find that spatial resolution affects the precision and accuracy of these lines. First, DEMs with

280   coarser resolution decrease the precision due to spatial averaging, blurring ridge topography by smoothing out peaks and saddles (Purinton and Bookhagen 2017). This effect may be more pronounced in SRTM data, which can have high errors on steep slopes and often poorly represent ridges and valley bottoms (Schwanghart and Scherler 2017; Gorokhovich and Voustianiouk 2006). Coarser resolution also biases, or decreases the accuracy of, our estimates because DEM values along ridges are lowered by spatial averaging (Fujita et al. 2008). Both effects entail that modelled shadow outlines on glaciers

285   increasingly lack detail and underestimate shadow length with coarser DEM resolution (Fig. 7). Poor quality of the underlying DEM will propagate into estimates of glacier elevation change. Satellite imagery obtained for the date of DEM acquisition can help quantify and correct for such biases.

Besides differences in resolution, the type of DEM also impacts the precision and accuracy of modelled shadows. Our analysis shows that among the DEMs with global coverage, the new GLO-30 DEM has the highest precision of derived

290 shadows when compared to the benchmark swissALTI3D DEM, which is consistent with recent DEM assessments that underscore the high performance of the GLO-30 DEM (Guth and Geoffroy 2021) (Fig. 7). Shadow outlines calculated from NASADEM and SRTM-1 are similar as they are obtained from the same data. We acknowledge that our method leaves any effects of SAR penetration into the snow pack atop the glacier ice uncorrected (Berthier et al. 2006). Snow cover can be thick in accumulation areas and may lead to biases (underestimates) when calculating glacier volume changes from DEM

295 differencing (Gardelle et al. 2012). Though most shadows in our cases are in the ablation zone, we recommend to account for differing penetration depth in future studies that also include shadows on glaciers at very high elevations. The relatively low performance of the AW3D30 DEM in comparison to other global DEMs likely relates to hillslope and ridge artifacts caused by errors in optical DEM generation (Purinton and Bookhagen 2017). In any case, our Bayesian framework objectively propagates these errors and uncertainties. One promising avenue for future research is to use narrower priors based on previous

300 research on glacier elevation change (Hugonnet et al. 2021) to further reduce uncertainty in the trends on glacier elevation changes.

In addition to the resolution and quality of the DEM, we expect that higher image resolution will warrant a higher precision at which elevation changes can be detected. We refrained from analyzing the effects of image resolution because we used only Landsat imagery with the longest freely available time series of satellite imagery. However, we recall that our

305 trigonometric approach hinges on sun elevation and image resolution provided in the image meta data, both setting the detection limit of elevation changes. For example, for a sun elevation of 20° and a spatial resolution of 30 m, a minimum elevation change of 10.9 m can be detected unless subpixel classification approaches or pan-sharpening techniques are adopted (Liu and Wu 2005). Sun angle will be critical for our method (Rada Giacaman 2022) and we expect that our approach works better for images acquired during the winter months of the respective hemispheres as well as at higher latitudes. To determine

310 interannual trends, we recommend using satellite imagery with similar time stamps within a year, given that glacier elevations are prone to seasonal variations (Moholdt et al. 2010).

Atmospheric refraction – the bending of solar light as it traverses the atmosphere – leads to an apparently higher sun elevation. The offset between the actual and apparent solar-position leads to errors in shadow-height applications depending mainly on solar elevation and, to a minor degree, on atmospheric pressure, humidity and temperature (Rada Giacaman 2022).

315 Sun elevations in our study range between 15 and 40° which yields height difference errors of 0-2% (see Fig. 10 in Rada Giacaman, 2022). Additional error sources include uncertainties in the position of the satellite as well as problems in image registration and deformation. Yet, we did not account for errors due to atmospheric refraction and image registration as they appear minor compared to those related to image resolution and DEM quality.

Our study reveals and confirms decadal-scale loss of glacier mass, which is consistent with independent estimates of

320 glacier elevation changes based on the data of McNeil et al. (2022) and historic topographic maps of the Great Aletsch Glacier (Fischer et al. 2015; Leinss and Bernhard 2021). For the Baltoro Glacier, we detect no credible trends and independent

validation data of surface changes at the shadow location are lacking. Yet, comparison of photographs from 1909 and 2004 show that glacier elevation changes at Concordia were low in the 20th century (<40 m) (Mayer et al. 2006). These small rates of surface lowering have been attributed to increases in precipitation and a lowering of summer mean and minimum

325 temperatures in the Karakoram, supporting regionally unchanged glacier masses referred to as 'Karakoram Anomaly' (Hewitt 2005; Kääb et al. 2015; Forsythe et al. 2017; Farinotti et al. 2020).

We stress that our results should not be compared directly with glacier-wide mass balances because these integrate over entire glaciers or elevation bands within glaciers whereas our results are representative for the shaded area only. We envision that our method could enhance, complement, and amend geodetic surveys in ablation and accumulation areas (Beedle

330 et al. 2014). Potentially, our method can be applied globally, but is restricted to those glaciers that are surrounded by steep topography producing sufficiently long cast shadows. Suitable sites remain to be identified and should, at best, have high-resolution DEMs with high precision and accuracy available. Locations with large landslides that lower mountain peaks (Shugar et al. 2021) should be avoided as they may violate the assumption of unaltered ridge topography over time. The processing steps developed in this study can be fully automated although quality control of the obtained geodetic lines

335 connecting modelled and actual shadow outlines are crucial.

5 Conclusions and outlook

In summary, our analysis shows that cast shadows offer avenues to retrieve ice-topographic changes from satellite imagery. We demonstrate for four glaciers that our method provides quantitative information about the change in glacier thickness over time that are consistent with independent DEMs of difference. The spatial resolution of the satellite imagery

340 from which shadows are retrieved, as well as the quality and resolution of DEMs is critical to the precision at which ice-topographic changes can be resolved. Upon the emergence of global, high-resolution DEMs with high precision, our method can be extended to historical satellite and aerial imagery under the assumption that the geometry of mountain ridges has not changed significantly by earth surface processes. We conclude that our approach has the potential to complement existing or future in situ measuring networks, providing data on ice-topographic changes especially for regions with limited access.

345

Appendix A: Additional tables

Table A1: Landsat bands used to map shadows on glaciers, including image metadata, the threshold to manually classify shadows on glaciers, and the number of geodetic lines that cross shadows on glaciers. TM: Thematic Mapper, ETM+: Enhanced Thematic Mapper, OLI: Operational Land Imager

Glacier	Acquisition Date	Landsat Mission	Band	Azimuth	Elevation	File Name in GeoTIFF format	Threshold between shadow and no-shadow	Number of geodetic lines drawn
Great Aletsch	06.02.1987	TM	2	146.964584	21.954781	LT05_L1TP_195028_19870206_20170213_01_T1_sr_band2	5500	106
Great Aletsch	18.02.1988	TM	2	147.489700	26.382202	LT05_L1TP_194028_19880218_20180215_01_T1_sr_band2	5500	106
Great Aletsch	11.02.1989	TM	2	148.324875	25.394554	LT05_L1TP_195028_19890211_20180215_01_T1_sr_band2	5500	105
Great Aletsch	07.02.1990	TM	2	146.875916	22.344643	LT05_L1TP_194028_19900207_20180219_01_T1_sr_band2	5500	105
Great Aletsch	01.02.1991	TM	2	147.642700	20.642624	LT05_L1TP_195028_19910201_20180215_01_T2_sr_band2	5500	101
Great Aletsch	06.02.1993	TM	2	147.113144	22.210066	LT05_L1TP_195028_19930206_20180215_01_T1_sr_band2	5500	106
Great Aletsch	25.02.1994	TM	2	144.214462	28.100639	LT05_L1TP_195028_19940225_20180215_01_T1_sr_band2	5500	100
Great Aletsch	21.02.1995	TM	2	142.355377	25.59594	LT05_L1TP_194028_19950221_20180215_01_T1_sr_band2	5500	102
Great Aletsch	21.02.1996	TM	2	142.074844	23.064941	LT05_L1TP_195028_19960215_20180215_01_T1_sr_band2	5500	102
Great Aletsch	01.02.1997	TM	2	148.578949	21.192062	LT05_L1TP_195028_19970201_20180215_01_T1_sr_band2	5500	108
Great Aletsch	20.02.1998	TM	2	148.899734	27.876671	LT05_L1TP_195028_19980220_20180215_01_T1_sr_band2	5500	105
Great Aletsch	10.02.2000	TM	2	149.530487	24.195702	LT05_L1TP_195028_20000210_20171211_01_T1_sr_band2	5500	106
Great Aletsch	14.02.2004	TM	2	150.348663	25.929115	LT05_L1TP_194028_20040214_20180311_01_T1_sr_band2	5500	107
Great Aletsch	07.02.2005	TM	2	153-035782	24.646736	LT05_L1TP_195028_20050207_20180130_01_T1_sr_band2	5500	107
Great Aletsch	10.02.2006	TM	2	153.752365	25.810577	LT05_L1TP_195028_20060210_20180311_01_T1_sr_band2	5500	107
Great Aletsch	22.02.2007	TM	2	153.493362	29.982136	LT05_L1TP_194028_20070222_20180118_01_T1_sr_band2	5500	106
Great Aletsch	18.02.2009	TM	2	151.651184	28.134636	LT05_L1TP_195028_20090218_20180302_01_T2_sr_band2	5500	109

Great Aletsch	21.02.2010	TM	2	152.591125	29.46365	LT05_L1TP_195028_20100221_20161016_01_T1_sr_band2	5500	108
Great Aletsch	08.02.2011	TM	2	153.846497	25.078377	LT05_L1TP_195028_20110208_20161010_01_T1_sr_band2	5500	109
Great Aletsch	25.02.2014	OLI	3	154.881790	31.66713	LC08_L1TP_194028_20140225_20170425_01_T1_sr_band3	5500	108
Great Aletsch	19.02.2015	OLI	3	155.215179	29.37574	LC08_L1TP_195028_20150219_20170412_01_T1_sr_band3	5500	107
Great Aletsch	15.02.2016	OLI	3	155.683655	27.952034	LC08_L1TP_194028_20160215_20170329_01_T1_sr_band3	5500	110
Great Aletsch	22.02.2019	OLI	3	155.717209	27.702271	LC08_L1TP_195028_20190214_20190222_01_T1_sr_band3	5500	113
Baltoro	11.02.1992	TM	3	141.603058	30.554222	LT05_L1TP_148035_19920211_20170123_01_T1_sr_band2	5500	49 when only using SRTM / 50 when using SRTM and VFP
Baltoro	22.02.1996	TM	3	135.052658	31.428848	LT05_L1TP_148035_19960222_20170105_01_T1_sr_band2	5000	40 / 42
Baltoro	24.01.2000	ETM+	2	151.93563529	29.47668300	LE07_L1TP_148035_20000124_20170213_01_T1_B2	200	57 / 58
Baltoro	15.02.2011	TM	2	147.356308	34.913021	LT05_L1TP_148035_20110215_20161010_01_T1_sr_band2	5000	35 / 38
Baltoro	10.02.2015	OLI	3	150.857864	34.447273	LC08_L1TP_148035_20150210_20170413_01_T1_sr_band3	4500	38 / 39
Baltoro	29.02.2016	OLI	3	147.819061	40.665691	LC08_L1TP_148035_20160229_20170329_01_T1_sr_band3	5000	26 / 30
Baltoro	02.02.2018	OLI	3	152.160034	32.333149	LC08_L1TP_148035_20180202_20180220_01_T1_sr_band3	5000	40 / 40
Baltoro	08.02.2020	OLI	3	151.290161	33.83334	LC08_L1TP_148035_20200208_20200211_01_T1_sr_band3	5000	40 / 40
Gulkana	14.03.2009	TM	2	162.214737	23.800697	LT05_L1TP_066016_20090314_20160906_01_T1_sr_band2	5500	179
Gulkana	06.03.2014	OLI	3	165.732956	17.113144	LC08_L1TP_066016_20140224_20170306_01_T1_sr_band3	6500	210
Gulkana	27.02.2015	OLI	3	165.491165	18.124138	LC08_L1TP_066016_20150227_20170227_01_T1_sr_band3	7500	210
Gulkana	21.02.2016	OLI	3	165.598206	15.814644	LC08_L1TP_067016_20160221_20170224_01_T1_sr_band3	7000	189
Gulkana	22.02.2019	OLI	3	165.540833	16.271332	LC08_L1TP_066016_20190222_20190308_01_T1_sr_band3	5500	215
Gulkana	25.02.2020	OLI	3	165.567917	17.298187	LC08_L1TP_066016_20200225_20200313_01_T1_sr_band3	6000	214
South Cascade	02.02.1987	TM	2	148.871033	18.89505	LT05_L1TP_046026_19870202_20161003_01_T1_sr_band2	5000	34
South Cascade	18.02.1993	TM	2	147.044220	23.976379	LT05_L1TP_046026_19930218_20160928_01_T1_sr_band2	5000	32
South Cascade	05.02.1994	TM	2	148.492279	19.785645	LT05_L1TP_046026_19940205_20160927_01_T1_sr_band2	5000	34

South Cascade	11.02.1996	TM	2	144.092560	20.011215	LT05_L1TP_046026_19960211_20160925_01_T1_sr_band2	5000	29
South Cascade	22.02.1997	TM	2	147.531799	25.733513	LT05_L1TP_045026_19970222_20160924_01_T1_sr_band2	5000	31
South Cascade	29.01.2000	ETM+	2	157.09748699	20.21436407	LE07_L1TP_046026_20000129_20161003_01_T1_B2	100	32
South Cascade	20.02.2002	TM	2	150.966492	25.979042	LT05_L1TP_045026_20020220_20160916_01_T1_sr_band2	5000	32
South Cascade	07.02.2003	TM	2	151.176193	21.319801	LT05_L1TP_045026_20030207_20160916_01_T2_sr_band2	5000	33
South Cascade	10.02.2004	TM	2	152.290070	22.594368	LT05_L1TP_045026_20040210_20160914_01_T2_sr_band2	5000	33
South Cascade	15.02.2006	TM	2	154.723404	25.245605	LT05_L1TP_045026_20060215_20160911_01_T1_sr_band2	5000	29
South Cascade	02.02.2007	TM	2	157.053238	21.438293	LT05_L1TP_045026_20070202_20160911_01_T1_sr_band2	5000	31
South Cascade	07.02.2009	TM	2	154.308121	22.459023	LT05_L1TP_045026_20090207_20160906_01_T1_sr_band2	5000	32
South Cascade	17.02.2010	TM	2	154.557983	25.933197	LT05_L1TP_046026_20100217_20160904_01_T1_sr_band2	5000	32
South Cascade	20.02.2011	TM	2	154.066223	26.817307	LT05_L1TP_046026_20110220_20160901_01_T1_sr_band2	5000	33
South Cascade	15.02.2015	OLI	3	157.108383	25.78627	LC08_L1TP_046026_20150215_20170301_01_T1_sr_band3	5000	28
South Cascade	13.02.2017	OLI	3	157.278580	25.300629	LC08_L1TP_045026_20170213_20180201_01_T2_sr_band3	5000	31
Sperry	28.02.1986	TM	2	147.031769	27.790085	LT05_L1TP_041026_19860228_20161004_01_T1_sr_band2	3500	33
Sperry	19.02.2000	TM	2	149.878403	25.038727	LT05_L1TP_041026_20000219_20160918_01_T1_sr_band2	3500	23
Sperry	27.02.2003	TM	2	149.099426	28.044254	LT05_L1TP_041026_20030227_20160916_01_T1_sr_band2	3500	33
Sperry	19.02.2006	TM	2	154.372833	26.612225	LT05_L1TP_041026_20060219_20160911_01_T1_sr_band2	3500	34
Sperry	25.02.2008	TM	2	153.742905	28.536865	LT05_L1TP_041026_20080225_20160906_01_T1_sr_band2	3500	30
Sperry	25.02.2014	OLI	3	156.529221	29.456596	LC08_L1TP_041026_20140225_20170307_01_T1_sr_band3	3500	33
Sperry	28.02.2015	OLI	3	156.081711	30.424019	LC08_L1TP_041026_20150228_20170301_01_T1_sr_band3	3500	33

350

Table A2: DEMs used to simulate shadows on glaciers, including spatial resolution, acquisition date, and data source.

DEM	Investigated Glacier	Spatial resolution [m]	Acquisition date	Source
swissALTI3D	Great Aletsch	(downsampled to 5m)	2017-2018	https://www.swisstopo.admin.ch/en/geodata/height/alti3d.html
Viewfinder Panoramas	Baltoro	30 m	diverse	http://viewfinderpanoramas.org/
ArcticDEM	Gulkana	2	2009	https://www.pgc.umn.edu/data/arcticdem/
SRTM-1	Great Aletsch, Baltoro, Gulkana, South Cascade, Sperry	~30 (1-Arc second)	2000	http://www.opentopography.org
SRTM-3	Great Aletsch	~90 (3-Arc seconds)	2000	http://www.opentopography.org
NASADEM	Great Aletsch	30	2000	http://www.opentopography.org
ALOS 3D World (AW3D30)	Great Aletsch	30	2006-2011	http://www.opentopography.org
Copernicus Global DEM (GLO-30)	Great Aletsch	30	2010-2015	http://www.opentopography.org
Copernicus Global DEM (GLO-90)	Great Aletsch	90	2010-2015	http://www.opentopography.org

355   **Table A3: Prior and posterior distributions of the parameters in the local models of glacier elevation change Δh with year y using geodetic lines (Eqs. 1-11).**

Parameter	Prior	Posterior Mean | 2.5% | 97.5% of HDI
α	Normal (mean = 0, sd = 2.5)	0.06 | -0.08| 0.21
β	Normal (mean = 0, sd = 2.5)	-0.32 | -0.88 | 0.25
σ_α	Normal (mean = 0, sd = 2.5) T(0,)	0.13 | 0.04 | 0.37
σ_β	Normal (mean = 0, sd = 2.5) T(0,)	0.54 | 0.22 | 1.39
κ	Normal (mean = 0, sd = 2.5) T(0,)	0.52 | 0.51 | 0.54
ς	LkjCholesky(1) on **R**	0.35 | -0.69 | 0.96

Notes: Priors refer to standardised input data pairs of Δh and y using a mean of zero and unit standard deviation. T($\cdot$, $\cdot$) indicates a truncation of the distribution at an lower or upper boundary. sd, standard deviation.

360 **Table A4: Prior and posterior distributions of the parameters in the local models of glacier elevation change Δh with year y using data from reference DEMs and historical maps (Eqs. 1-11).**

Parameter	Prior	Posterior for all available data Mean | 2.5% | 97.5% of HDI	Posterior for data from the Landsat era only Mean | 2.5% | 97.5% of HDI
α	Normal (mean = 0, sd = 2.5)	0.18 | -1.05| 1.42	0.22 | -1.14| 1.56
β	Normal (mean = 0, sd = 2.5)	-0.55 | -1.25 | 0.18	-0.43 | -0.99| 0.23
σ_α	Normal (mean = 0, sd = 2.5) T(0,)	1.12 | 0.42 | 2.85	1.27 | 0.48 | 3.13
σ_β	Normal (mean = 0, sd = 2.5) T(0,)	0.6 | 0.17 | 1.81	0.36 | -0.01 | 1.58
κ	Normal (mean = 0, sd = 2.5) T(0,)	0.27 | 0.18 | 0.4	0.24 | 0.12 | 0.45
ς	LkjCholesky(1) on **R**	0.37 | -0.68 | 0.97	-0.07 | -0.94 | 0.92

Notes: Priors refer to standardised input data pairs of Δh and y using a mean of zero and unit standard deviation. T(· , ·) indicates a truncation of the distribution at an lower or upper boundary. sd, standard deviation.

Data and code availability

365 The outlines of the shadows, the geodetic lines, tables with inferred elevation changes for each glacier, and the Bayesian multi-level models are available via *Zenodo* (https://doi.org/10.5281/zenodo.7134743). Landsat images were obtained from *EarthExplorer* (https://usgs.earthexplorer.gov), and all DEMs are freely available from the sources provided in Table A2. Codes to fit the Bayesian multi-level models are available at *GitHub* (https://github.com/geveh/ShadowsOnGlaciers).

Author contributions

370 All authors contributed equally in designing the study, conducting the analysis, validating the results, and writing the manuscript.

Competing interests

The authors declare that they have no conflict of interest.

Acknowledgements

Publication bibliography

380 Azam, M. F.; Kargel, J. S.; Shea, J. M.; Nepal, S.; Haritashya, U. K.; Srivastava, S. et al.: Glaciohydrology of the Himalaya-Karakoram, *Science (New York, N.Y.)* 373 (6557), doi: 10.1126/science.abf3668, 2021.

Bauder, A.; Funk, M.; Huss, M.: Ice-volume changes of selected glaciers in the Swiss Alps since the end of the 19th century, *Ann. Glaciol.* 46, pp. 145–149, doi: 10.3189/172756407782871701, 2007.

Beedle, M. J.; Menounos, B.; Wheate, R.: An evaluation of mass-balance methods applied to Castle creek Glacier, British
385 Columbia, Canada, *J. Glaciol.* 60 (220), pp. 262–276, doi: 10.3189/2014JoG13J091, 2014.

Berthier, E.; Arnaud, Y.; Vincent, C.; Rémy, F.: Biases of SRTM in high-mountain areas: Implications for the monitoring of glacier volume changes, *Geophys. Res. Lett.* 33 (8), doi: 10.1029/2006GL025862, 2006.

Bolch, T.; Pieczonka, T.; Benn, D. I.: Multi-decadal mass loss of glaciers in the Everest area (Nepal Himalaya) derived from stereo imagery, *The Cryosphere* 5 (2), pp. 349–358, doi: 10.5194/tc-5-349-2011, 2011.

390 Brighenti, S.; Tolotti, M.; Bruno, M. C.; Wharton, G.; Pusch, M. T.; Bertoldi, W.: Ecosystem shifts in Alpine streams under glacier retreat and rock glacier thaw: A review, *The Science of the total environment* 675, pp. 542–559, doi: 10.1016/j.scitotenv.2019.04.221, 2019.

Bürkner, P. C.: brms: An R Package for Bayesian Multilevel Models Using Stan, *J. Stat. Soft.* 80 (1), doi: 10.18637/jss.v080.i01, 2017.

395 Cauvy-Frauníé, S.; Dangles, O.: A global synthesis of biodiversity responses to glacier retreat, *Nature ecology & evolution* 3 (12), pp. 1675–1685, doi: 10.1038/s41559-019-1042-8, 2019.

Conrad, O.; Bechtel, B.; Bock, M.; Dietrich, H.; Fischer, E.; Gerlitz, L. et al.: System for Automated Geoscientific Analyses (SAGA) version 2.1.4, *Geosci. Model Dev.* 8 (7), pp. 1991–2007, doi: 10.5194/gmd-8-1991-2015, 2015.

De Ferranti, J.: Digital Elevation Data: SRTM Void Fill. Viewfinder Panoramas, available online at
400 *http://www.viewfinderpanoramas.org/voidfill.html*, updated on 12/21/2015, checked on 8/28/2022, 2015.

Farías-Barahona, D.; Sommer, C.; Sauter, T.; Bannister, D.; Seehaus, T. C.; Malz, P. et al.: Detailed quantification of glacier elevation and mass changes in South Georgia, *Environ. Res. Lett.* 15 (3), p. 34036, doi: 10.1088/1748-9326/ab6b32, 2020.

Farinotti, D.; Huss, M.; Fürst, J. J.; Landmann, J.; Machguth, H.; Maussion, F.; Pandit, A.: A consensus estimate for the ice thickness distribution of all glaciers on Earth, *Nat. Geosci.* 12 (3), pp. 168–173, doi: 10.1038/s41561-019-0300-3, 2019.

405 Farinotti, D.; Immerzeel, W. W.; De Kok, R.; Quincey, D. J.; Dehecq, A.: Manifestations and mechanisms of the Karakoram glacier Anomaly, *Nature geoscience* 13 (1), pp. 8–16, doi: 10.1038/s41561-019-0513-5, 2020.

Farr, T. G.; Rosen, P. A.; Caro, E.; Crippen, R.; Duren, R.; Hensley, S. et al.: The Shuttle Radar Topography Mission, *Rev. Geophys.* 45 (2), doi: 10.1029/2005RG000183, 2007.

The Cryosphere
Discussions
Open Access
EGU

Fischer, M.; Huss, M.; Hoelzle, M.: Surface elevation and mass changes of all Swiss glaciers 1980–2010, *The Cryosphere* 9 (2), pp. 525–540, doi: 10.5194/tc-9-525-2015, 2015.

Forsythe, N.; Fowler, H. J.; Li, X. F.; Blenkinsop, S.; Pritchard, D.: Karakoram temperature and glacial melt driven by regional atmospheric circulation variability, *Nature Clim Change* 7 (9), pp. 664–670, doi: 10.1038/nclimate3361, 2017.

Fujita, K.; Suzuki, R.; Nuimura, T.; Sakai, A.: Performance of ASTER and SRTM DEMs, and their potential for assessing glacial lakes in the Lunana region, Bhutan Himalaya, *J. Glaciol.* 54 (185), pp. 220–228, doi: 10.3189/002214308784886162, 2008.

Gardelle, J.; Berthier, E.; Arnaud, Y.: Impact of resolution and radar penetration on glacier elevation changes computed from DEM differencing, *J. Glaciol.* 58 (208), pp. 419–422, doi: 10.3189/2012JoG11J175, 2012.

Gorokhovich, Y.; Voustianiouk, A.: Accuracy assessment of the processed SRTM-based elevation data by CGIAR using field data from USA and Thailand and its relation to the terrain characteristics, *Remote Sensing of Environment* 104 (4), pp. 409–415, doi: 10.1016/j.rse.2006.05.012, 2006.

Guth, P. L.; Geoffroy, T. M.: LiDAR point cloud and ICESat-2 evaluation of 1 second global digital elevation models: Copernicus wins, *Transactions in GIS* 25 (5), pp. 2245–2261, doi: 10.1111/tgis.12825, 2021.

Hewitt, K.: The Karakoram Anomaly? Glacier Expansion and the 'Elevation Effect,' Karakoram Himalaya, *Mountain Research and Development* 25 (4), pp. 332–340, doi: 10.1659/0276-4741(2005)025[0332:TKAGEA]2.0.CO;2, 2005.

Huggel, C.; Clague, J. J.; Korup, O.: Is climate change responsible for changing landslide activity in high mountains?, *Earth Surf. Process. Landforms* 37 (1), pp. 77–91, doi: 10.1002/esp.2223, 2012.

Hugonnet, R.; McNabb, R.; Berthier, E.; Menounos, B.; Nuth, C.; Girod, L. et al.: Accelerated global glacier mass loss in the early twenty-first century, *Nature* 592 (7856), pp. 726–731, doi: 10.1038/s41586-021-03436-z, 2021.

IPCC: Special Report on the Ocean and Cryosphere in a Changing Climate, edited by H.-O. Pörtner,D.C. Roberts, V. Masson-Delmotte, P. Zhai, M. Tignor, E. Poloczanska, K. Mintenbeck, A. Alegría, M. Nicolai, A. Okem, J. Petzold, B. Rama, N.M. Weyer, available online at https://www.ipcc.ch/srocc/, checked on 8/28/2022, 2019.

Kääb, A.; Treichler, D.; Nuth, C.; Berthier, E.: Brief Communication: Contending estimates of 2003–2008 glacier mass balance over the Pamir–Karakoram–Himalaya, *The Cryosphere* 9 (2), pp. 557–564, doi: 10.5194/tc-9-557-2015, 2015.

Kääb, A.; Winsvold, S.; Altena, B.; Nuth, C.; Nagler, T.; Wuite, J.: Glacier Remote Sensing Using Sentinel-2. Part I: Radiometric and Geometric Performance, and Application to Ice Velocity, *Remote Sensing* 8 (7), p. 598, doi: 10.3390/rs8070598, 2016.

Kruschke, J.: Doing Bayesian data analysis. A tutorial with R, JAGS, and Stan, 2nd ed.: Elsevier, 2014.

Leinss, S.; Bernhard, P.: TanDEM-X:Deriving InSAR Height Changes and Velocity Dynamics of Great Aletsch Glacier, *IEEE J. Sel. Top. Appl. Earth Observations Remote Sensing* 14, pp. 4798–4815, doi: 10.1109/JSTARS.2021.3078084, 2021.

Li, D.; Lu, X.; Overeem, I.; Walling, D. E.; Syvitski, J.; Kettner, A. J. et al.: Exceptional increases in fluvial sediment fluxes in a warmer and wetter High Mountain Asia, *Science (New York, N.Y.)* 374 (6567), pp. 599–603, doi: 10.1126/science.abi9649, 2021.

Li, H.; Xu, L.; Shen, H.; Zhang, L.: A general variational framework considering cast shadows for the topographic correction of remote sensing imagery, *ISPRS Journal of Photogrammetry and Remote Sensing* 117, pp. 161–171, doi: 10.1016/j.isprsjprs.2016.03.021, 2016.

Liu, W.; Wu, E. Y.: Comparison of non-linear mixture models: sub-pixel classification, *Remote Sensing of Environment* 94 (2), pp. 145–154, doi: 10.1016/j.rse.2004.09.004, 2005.

Mayer, C.; Lambrecht, A.; Belò, M.; Smiraglia, C.; Diolaiuti, G.: Glaciological characteristics of the ablation zone of Baltoro glacier, Karakoram, Pakistan, *Annals of Glaciology* 43, pp. 123–131, doi: 10.3189/172756406781812087, 2006.

450   McElreath, R.: Statistical Rethinking: Chapman and Hall/CRC, 2020.

McNeil, C. J.; Florentine, C. E.; Bright, V. A. L.; Fahey, M. J.; McCann, E.; Larsen, C. F. et al.: Geodetic Data for USGS Benchmark Glaciers: Orthophotos, Digital Elevation Models, Glacier Boundaries and Surveyed Positions, version 2.0, *US Geological Survey data release*, doi: 10.5066/P9R8BP3K, 2022.

Millan, R.; Mouginot, J.; Rabatel, A.; Morlighem, M.: Ice velocity and thickness of the world's glaciers, *Nature geoscience* 455   15 (2), pp. 124–129, doi: 10.1038/s41561-021-00885-z, 2022.

Milner, A. M.; Khamis, K.; Battin, T. J.; Brittain, J. E.; Barrand, N. E.; Füreder, L. et al.: Glacier shrinkage driving global changes in downstream systems, *Proceedings of the National Academy of Sciences of the United States of America* 114 (37), pp. 9770–9778, doi: 10.1073/pnas.1619807114, 2017.

Minora, U.; Senese, A.; Bocchiola, D.; Soncini, A.; D'agata, C.; Ambrosini, R. et al.: A simple model to evaluate ice melt 460   over the ablation area of glaciers in the Central Karakoram National Park, Pakistan, *Annals of Glaciology* 56 (70), pp. 202–216, doi: 10.3189/2015AoG70A206, 2015.

Moholdt, G.; Nuth, C. Hagen, J. O.; Kohler, J.: Recent elevation changes of Svalbard glaciers derived from ICESat laser altimetry, *Remote Sensing of Environment* 114 (11), pp. 2756–2767, doi: 10.1016/j.rse.2010.06.008, 2010.

Mukul, M.; Srivastava, V.; Jade, S.; Mukul, M.: Uncertainties in the Shuttle Radar Topography Mission (SRTM) Heights: 465   Insights from the Indian Himalaya and Peninsula, *Scientific reports* 7, p. 41672, doi: 10.1038/srep41672, 2017.

Neckel, N.; Kropáček, J.; Bolch, T.; Hochschild, V.: Glacier mass changes on the Tibetan Plateau 2003–2009 derived from ICESat laser altimetry measurements, *Environ. Res. Lett.* 9 (1), p. 14009, doi: 10.1088/1748-9326/9/1/014009, 2014.

Paul, F.; Andreassen, L. M.; Winsvold, S. H.: A new glacier inventory for the Jostedalsbreen region, Norway, from Landsat TM scenes of 2006 and changes since 1966, *Ann. Glaciol.* 52 (59), pp. 153–162, doi: 10.3189/172756411799096169, 2011.

470   Paul, F.; Kääb, A.; Maisch, M.; Kellenberger, T.; Haeberli, W., International Glaciological Society: The new remote-sensing-derived Swiss glacier inventory: I. Methods, *Ann. Glaciol.* (34), 355 - 361, 2002.

Pfeffer, W. Tad; Arendt, Anthony A.; Bliss, Andrew; Bolch, Tobias; Cogley, J. Graham; Gardner, Alex S. et al.: The Randolph Glacier Inventory: A globally complete inventory of glaciers, *J. Glaciol.* 60 (No. 221), pp. 537–552, doi: 10.3189/2014JoG13J176, 2014.

475   Pritchard, H. D.: Asia's shrinking glaciers protect large populations from drought stress, *Nature* 569 (7758), pp. 649–654, doi: 10.1038/s41586-019-1240-1, 2019.

Purinton, B.; Bookhagen, B.: Validation of digital elevation models (DEMs) and comparison of geomorphic metrics on the southern Central Andean Plateau, *Earth Surface Dynamics* 5 (2), pp. 211–237, doi: 10.5194/esurf-5-211-2017, 2017.

R Core Team: R: The R Project for Statistical Computing, Vienna, Austria, available online at *https://www.r-project.org/*, 480   updated on 6/23/2022, checked on 8/17/2022, 2022.

Racoviteanu, A.; Williams, M. W.: Decision Tree and Texture Analysis for Mapping Debris-Covered Glaciers in the Kangchenjunga Area, Eastern Himalaya, *Remote Sensing* 4 (10), pp. 3078–3109, doi: 10.3390/rs4103078, 2012.

Rada Giacaman, C. A.: High-Precision Measurement of Height Differences from Shadows in Non-Stereo Imagery: New Methodology and Accuracy Assessment, *Remote Sensing* 14 (7), p. 1702, doi: 10.3390/rs14071702, 2022.

485 Rankl, M.; Braun, M.: Glacier elevation and mass changes over the central Karakoram region estimated from TanDEM-X and SRTM/X-SAR digital elevation models, *Ann. Glaciol.* 57 (71), pp. 273–281, doi: 10.3189/2016AoG71A024, 2016.

Richardson, S. D.; Reynolds, J. M.: An overview of glacial hazards in the Himalayas, *Quaternary International* 65-66, pp. 31–47, doi: 10.1016/S1040-6182(99)00035-X, 2000.

Richter, R.: Correction of satellite imagery over mountainous terrain, *Applied optics* 37 (18), pp. 4004–4015, 490 doi: 10.1364/AO.37.004004, 1998.

Schwanghart, W.; Scherler, D.: Bumps in river profiles: uncertainty assessment and smoothing using quantile regression techniques, *Earth Surf. Dynam.* 5 (4), pp. 821–839, doi: 10.5194/esurf-5-821-2017, 2017.

Shugar, D. H.; Jacquemart, M.; Shean, D.; Bhushan, S.; Upadhyay, K.; Sattar, A. et al.: A massive rock and ice avalanche caused the 2021 disaster at Chamoli, Indian Himalaya, *Science (New York, N.Y.)* 373 (6552), pp. 300–306, 495 doi: 10.1126/science.abh4455, 2021.

Stan Development Team: Stan Modeling Language Users Guide and Reference Manual, version 2.30, available online at *https://mc-stan.org/*, updated on 7/2/2022, checked on 8/17/2022, 2022.

Veh, G.; Korup, O.; Walz, A.: Hazard from Himalayan glacier lake outburst floods, *Proceedings of the National Academy of Sciences of the United States of America* 117 (2), pp. 907–912, doi: 10.1073/pnas.1914898117, 2020.

500 Wulder, M. A.; Loveland, T. R.; Roy, D. P.; Crawford, C. J.; Masek, J. G.; Woodcock, C. E. et al.: Current status of Landsat program, science, and applications, *Remote Sensing of Environment* 225, pp. 127–147, doi: 10.1016/j.rse.2019.02.015, 2019.

Wulder, M. A.; Roy, D. P.; Radeloff, V. C.; Loveland, T. R.; Anderson, M. C.; Johnson, D. M. et al.: Fifty years of Landsat science and impacts, *Remote Sensing of Environment* 280, p. 113195, doi: 10.1016/j.rse.2022.113195, 2022.

Zemp, M.; Hoelzle, M.; Haeberli, W.: Distributed modelling of the regional climatic equilibrium line altitude of glaciers in 505 the European Alps, *Global and Planetary Change* 56 (1-2), pp. 83–100, doi: 10.1016/j.gloplacha.2006.07.002, 2007.

Zhang, Z.; Xu, J. l.; Liu, S. Y.; Guo, W. Q.; Wei, J. F.; Feng, T.: Glacier changes since the early 1960s, eastern Pamir, China, *J. Mt. Sci.* 13 (2), pp. 276–291, doi: 10.1007/s11629-014-3172-4, 2016.